Renewable Energy 276 (2026) 126447

Contents lists available at ScienceDirect

Renewable Energy

journal homepage: www.elsevier.com/locate/renene

Impact of circumsolar irradiance and aerosol optical depth on CAMS surface solar irradiance estimates

Yehia Eissa [a,*], Yves-Marie Saint-Drenan [a], Marion Schroedter-Homscheidt [b], Antti Arola [c], Philippe Blanc [a]

[a] Mines Paris, Université PSL, Centre Observation Impacts Energie (O.I.E.), Sophia Antipolis, 06904, France
[b] German Aerospace Center (DLR), Institute of Networked Energy Systems, Oldenburg, Germany
[c] Finnish Meteorological Institute (FMI), Kuopio, Finland

ARTICLE INFO

Keywords:
BSRN
Copernicus
Direct
Normal irradiance
Pyranometer
Pyrheliometer

ABSTRACT

The global horizontal irradiance is a main variable in the integration of solar energy systems in electricity grids, and in climate and weather studies. The physical model McClear is the clear-sky module for the all-sky irradiance retrievals from the CAMS Radiation Service. Validations of McClear against high-quality in situ measurements reveal very accurate global horizontal irradiance estimates with negligible bias. Albeit still good, the beam and diffuse irradiance components exhibit biases generally opposing each other. These biases are mainly attributed to the aerosol optical depth used as input to McClear, and the forward scattered circumsolar irradiance surrounding the solar disc which is not modelled by McClear but intercepted within the solid angle aperture of radiometers measuring beam irradiance (and blocked by those measuring diffuse irradiance). This study performs a global scale validation of a desert-based circumsolar correction, and evaluates the influence of this circumsolar correction and the aerosol optical depth on the beam and diffuse irradiance estimates from McClear. Circumsolar corrected retrievals are enhanced globally, especially for the diffuse component of McClear, with the standard deviation of deviations improving from 26.3 to 24.4%, the bias from 19.0 to 13.1%, and the correlation remaining constant at 0.837. Comparing ground measured and CAMS modelled aerosol optical depth, improvements are expected with further developments to the CAMS aerosol model.

1. Introduction

Data of the downwelling surface solar irradiance, abbreviated as DSSI, is important in different fields, including solar energy technologies [1], indeed it is classified as an Essential Climate Variable for renewable energies [2]. The DSSI is the hemispherical downwelling solar irradiance received on a horizontal plane at the surface of the earth and integrated over the full electromagnetic spectrum, i.e., broadband value. DSSI data also supports national policymaking, as well as the needs of commercial and public sector services involved in planning, monitoring, enhancing efficiency and integration of solar energy systems into power grids [3]. It is also known as the global horizontal irradiance and abbreviated as GHI.

The GHI is composed of beam (or direct) and diffuse components. The beam normal irradiance, abbreviated as BNI, is the broadband irradiance originating from a small solid angle centered to the position of the Sun and received on a plane normal to the Sun, as defined in ISO 9488:2022. It comprises the irradiance from within the extent of the solar disc, having an angular radius of $0.266° \pm 1.7\%$ for an observer on earth, and the circumsolar normal irradiance (CSNI) from the larger circumsolar region surrounding the disc [4]. The extent of the CSNI is defined by the aperture solid angle, and it may be measured [5], or modelled with a magnitude dependent on the atmospheric conditions [6]. The World Meteorological Organization (WMO) recommends pyrheliometers measuring the BNI to have an aperture half-angle of 2.5° [7]. However, since not all field-deployed ones adhere to this recommendation, following Blanc et al. [4] it is advised to report information on the aperture solid angle with BNI measurements. The beam horizontal irradiance, abbreviated as BHI, is the component of the BNI received on the horizontal plane. The diffuse horizontal irradiance, abbreviated as DHI, is the scattered hemispherical downwelling solar broadband irradiance received on a horizontal plane at the surface of the earth. Measurements of the DHI exclude the circumsolar horizontal irradiance (CSHI), ideally from the same small solid angle of the BNI

* Corresponding author.
E-mail address: yehia.eissa@minesparis.psl.eu (Y. Eissa).

https://doi.org/10.1016/j.renene.2026.126447
Received 19 May 2026; Received in revised form 8 September 2026; Accepted 10 September 2026
Available online 11 September 2026
0960-1481/© 2026 The Authors. Published by Elsevier Ltd. This is an open access article under the CC BY license (http://creativecommons.org/licenses/by/4.0/).

measurements. These variables are related together by:

$$GHI = BNI(\alpha)\cos(\theta_S) + DHI^{exp}, \quad (1)$$

$$DHI^{exp} = DHI^{total} - CSHI(\alpha), \quad (2)$$

where *BNI* represents the modelled or measured BNI from the solid angle with aperture half-angle α, θ_S is the solar zenith angle, and the term $BNI(\alpha)\cos(\theta_S)$ corresponds to the horizontal component $BHI(\alpha)$. DHI^{exp} represents the modelled or measured DHI, i.e., excluding the $CSHI(\alpha)$ from the diffuse radiation from the whole sky DHI^{total}.

One requiring solar resource data would rely on continuous, high-quality in situ measurements of the GHI and its components. However, such measurements are scarce in time and space due to several practical limitations, including the high cost of instrumentation, need for regular maintenance and calibration, constraints on suitable installation sites that are accessible (e.g., unobstructed horizons and minimal local shading for solar radiometers), and challenges related to data acquisition, processing, and quality control. Therefore, in the absence of measurements at a site of interest, one will resort to models providing such data. Various models have been developed and validated for this purpose, where the modelling of the solar irradiance will normally be split into two separate modules [1]. One to model the clear-sky (or cloud-free) irradiance [8,9], and the other to model the attenuation due to the presence of clouds [10].

Focusing on the cloud-free module, as the extraterrestrial solar irradiance penetrates and traverses through the atmosphere, it interacts with several atmospheric constituents causing its attenuation through scattering and absorption processes. These constituents mainly comprise the: molecular gases responsible for Rayleigh scattering, ozone, water vapor and aerosols. Aerosols, in particular, vary in composition and loadings on the temporal and spatial scales. Therefore, detailed knowledge of the aerosol optical properties is essential for accurately characterizing their impact on the attenuation of the cloud-free GHI and its components [11].

The Copernicus Atmosphere Monitoring Service (CAMS), implemented by the European Centre for Medium-Range Weather Forecasts (ECMWF), provides open-access GHI, BNI, BHI and DHI data for cloud-free and all-sky conditions via its widely used CAMS Radiation Service [12]. It is based on McClear [13], a clear-sky model mimicking the radiative transfer code libRadtran [14,15] based on a look-up tables approach and interpolation functions using a given set of inputs describing the atmospheric conditions, vertical profiles of atmosphere, solar geometry, surface reflectance properties, and site characteristics. To date, McClear does not account for the circumsolar irradiance in its estimates.

Tables A.1 and A.2 in the appendix present the validations of McClear for global and beam irradiance from several studies, summarized by the root mean square error (RMSE), the bias, their relative values normalized by the mean reference values, and the correlation coefficient (CC). Quarterly evaluation and quality assurance, currently covering around 40 stations worldwide for McClear, are also published regularly on the CAMS Radiation Service website [12]. McClear performs very well [16], and several studies have compared its performance to other state-of-the-art models and agree that its performance is indeed very good [17,18].

The main source of error of the McClear global and beam irradiance is attributed to the CAMS aerosol optical depth (AOD) used by the model [13]. Similarly, studies involving other models report the AOD as the variable of most significance in their respective performance assessments [19]. For example, Salamalikis et al. [20] performed site specific calibrations of the CAMS AOD and reported significant improvements in the error metrics of the modelled BNI with the calibrations. Furthermore, Abreu et al. [21] evaluated libRadtran, SMARTS [22] and REST2 [9] to estimate the GHI and BNI using three input sources for the AOD and total column content in water vapor (one from a ground-based Sun photometer and two gridded reanalysis datasets). The coefficient of determination and the standard deviation of deviations were always better when using inputs of ground reference data. Sensitivity analysis showed that errors in the AOD and Ångström exponent affect the GHI and BNI more than errors in water vapor.

Another variable affecting the modelling of cloud-free BNI and DHI is circumsolar irradiance. On the one hand, BNI modelled by libRadtran, and McClear, treats the solar disc as a Dirac-delta function and does not include the CSNI. Therefore, McClear BNI is expected to be underestimated since pyrheliometers measure forward-direction scattered irradiance from a larger circumsolar region. On the other hand, McClear DHI includes the CSHI, since the scattered radiation from the whole sky is included in libRadtran simulations. Therefore, an overestimation of McClear DHI is expected, since measured values exclude the circumsolar region, normally with a shading ball or ring.

Not accounting for the circumsolar irradiance in the BNI estimates of McClear has been reported as a potential source of error [13], with no proposed solutions. Abreu et al. [21] do account for the CSNI when using the SMARTS model for BNI estimates and present results with and without the circumsolar irradiance. In the case with circumsolar irradiance there is expectedly an increase in bias, but more importantly the coefficient of determination is larger and the standard deviation of deviations is smaller when it is included, indicating an improvement in modelled values. Several extensions of circumsolar irradiance retrieval methods based on physical radiative transport modelling were proposed, ranging from satellite-based approaches and physics-based all-sky models [23,24], to simplified operational schemes under clear-sky conditions [25,26].

In this work the model of Eissa et al. [25] was selected because it requires only the beam and diffuse irradiances as inputs, unlike that of Elias et al. [26] which additionally requires the AOD. It is also developed for cloud-free conditions, which is the focus of this work. While Eissa et al. demonstrated the effectiveness of their circumsolar correction model at two desert sites, its global validation across diverse climate regions and aerosol types remains unexplored.

Therefore, the objective of this study is to perform a global scale validation of the Eissa et al. circumsolar model beyond its original development context, and evaluate the influence of this circumsolar correction and CAMS AOD uncertainties on the BNI and DHI estimates from the clear-sky McClear model of the operational CAMS Radiation Service.

The study addresses the following questions:

i. Can the parametric model of Eissa et al., which provides the CSNI and was originally developed for cloud-free desert environments, be applied effectively in diverse geographical settings with different aerosol characteristics?
ii. If so, to what extent does the circumsolar irradiance correction improve McClear BNI and DHI estimates at a global scale?
iii. What is the influence of the inherent errors in CAMS AOD on the performance of McClear?

A dataset was constructed comprising high-quality GHI, BNI and DHI measurements from the Baseline Surface Radiation Network (BSRN) from 24 stations [27], their corresponding McClear estimates, and co-located Sun photometer measurements of the Aerosol Robotic Network (AERONET) stations providing the reference aerosol optical properties [28]. A stringent cloud-free detection algorithm was applied to retain only such instances in the analysis. The circumsolar model of Eissa et al. [25] was then applied and integrated with the McClear estimates to evaluate its global validation, and the effect of such variable on the performance of McClear. Subsequently, the effects of the errors in the AOD with the errors of the GHI, BNI and DHI were evaluated.

This article is structured as follows: Sect. 2 describes the data sources, their quality, and the temporal and spatial matching between data of different sources, Sect. 3 presents the results and discussion, and Sect.

4 presents the conclusion and prospects.

2. Data and methods

The selection of stations was based on the availability of reference measurements of AOD and co-located high-quality solar irradiance measurements. AERONET stations were selected for retrieval of the AOD data, while solar irradiance measurements were obtained from BSRN stations. A threshold that co-located measurements be no more than 500 m apart was applied. For sample matching with McClear, only stations with overlapping ground measurements after 2004 were retained, resulting in a total of 24 stations (Table 1). The stations are globally distributed, with all continents represented except Antarctica, as shown in Fig. 1.

As dust aerosols cause a large part of the circumsolar effect in a cloud-free atmosphere, the contribution of dust was characterized by the ratio of mean dust AOD to mean total AOD as modelled by the CAMS Integrated Forecasting System composition module (IFS-COMPO, [30]), which provides global aerosol properties and is used as input to the McClear model. This ratio is also a mean to characterize the performance of the circumsolar correction in non-desert settings.

2.1. AERONET data

AERONET stations comprise an automatic Sun and sky scanning radiometer, namely the sun photometer model CIMEL Electronique CE-318. It collects direct Sun measurements with a 1.2° full field of view every ~5 to 15 min to provide the AOD at eight wavelengths (sometimes less for older instruments), and the total column content in water vapor [28]. Data from the Version 3 Direct Sun Algorithm product was

Table 1
Details of the stations used in this study. Stations are sorted from smallest to largest ratio of mean dust AOD versus mean total AOD derived from CAMS IFS-COMPO. The table includes station coordinates, altitude above mean sea level, Köppen-Geiger climate classification [29], number of available data points and the dust-to-total AOD ratio computed for the matched samples.

BSRN Abbreviation AERONET name	Country	Köppen-Geiger classification/ climate zone	mean dust AOD/mean total AOD	BSRN			# of matched samples
				Latitude (°N)	Longitude (°E)	Altitude (m)	
BRB Brasilia_SONDA	Brazil	Aw/Tropical	0.002	−15.601	−47.713	1023	843
MAN Manus	Papua New Guinea	Af/Tropical	0.005	−2.058	147.425	6	913
RUN REUNION_ST_DENIS	Reunion	Ocean/Ocean	0.005	−20.901	55.484	116	21571
NAU Nauru	Nauru	Ocean/Ocean	0.006	−0.521	166.917	7	437
LER Lerwick_MO	United Kingdom	Cfb/Temperate	0.007	60.139	−1.185	80	73
SMS Sao_Martinho_SONDA	Brazil	Cfa/Temperate	0.009	−29.443	−53.823	489	11748
NYA Ny_Alesund_AWI	Norway	ET/Polar	0.009	78.923	11.927	11	12172
GIM Granite_Island	USA	Dfb/Continental	0.010	46.721	−87.411	208	14747
EUR (Eureka) OPAL	Canada	ET/Polar	0.012	79.989	−85.940	85	21672
TIK Tiksi	Russia	Dsd/Continental	0.015	71.586	128.919	48	1082
DAR Darwin	Australia	Aw/Tropical	0.017	−12.425	130.891	30	859
REG (Regina) Bratts_Lake	Canada	Dfb/Continental	0.019	50.205	−104.713	578	17964
BON BONDVILLE	USA	Cfa/Temperate	0.021	40.067	−88.367	213	31619
PTR Petrolina_SONDA	Brazil	BSh/Dry	0.033	−9.069	−40.320	387	9083
CAB Cabauw	Netherlands	Cfb/Temperate	0.044	51.968	4.928	0	14773
BOS (Boulder) Table_Mountain	USA	BSk/Dry	0.054	40.125	−105.237	1689	47152
LIN MetObs_Lindenberg	Germany	Cfb/Temperate	0.059	52.210	14.122	125	25682
E13 (Southern Great Plains) ARM_SGP	USA	Cfa/Temperate	0.077	36.605	−97.485	318	17466
PAY Payerne	Switzerland	Cfb/Temperate	0.082	46.812	6.942	491	28891
CAR Carpentras	France	Csa/Temperate	0.090	44.083	5.059	100	57699
CNR CENER	Spain	Cfb/Temperate	0.117	42.816	−1.601	471	15806
ENA (Eastern North Atlantic) ARM_Graciosa	Portugal	Ocean/Ocean	0.122	39.091	−28.029	15	1286
XIA XiangHe	China	BSk/Dry	0.151	39.754	116.962	32	20687
GOB Gobabeb	Namibia	BWh/Dry	0.349	−23.561	15.042	407	235953



Fig. 1. Map of the world showing the geographic locations of the 24 stations (https://umap.openstreetmap.fr/).

downloaded, all in Level 2 to ensure quality-assured and cloud-screened data.

AERONET AOD is not provided at the exact wavelength of 550 nm as used as input to the McClear model. Therefore, to match between the different sources in terms of wavelength, the method of King and Byrne [31] was applied to the measurements at each timestamp by utilizing a second-order polynomial fit as:

$$\ln \tau_{a,\lambda} = a_0 + a_1 \ln \lambda + a_2 (\ln \lambda)^2, \quad (3)$$

where $\tau_{a,\lambda}$ is the AOD at wavelength λ, and a_0, a_1 and a_2 are the fitting coefficients. This method was chosen to account for the curvature in ln $\tau_{a,\lambda}$ versus ln λ [32]. There must be at least 3 AOD measurements at different wavelengths present at the timestamp to apply Eq. (3).

2.2. BSRN data

Measurements of the BSRN network are collected using Class A thermopiles, and the GHI, BNI and DHI are measured using separate radiometers. They are available as 1-min averages at all 24 stations. The pyrheliometers used for BNI measurements have aperture half-angles of either 2.5° or 2.9°. The quality-control tests presented in Sengupta et al. [1] were applied to filter any suspicious reference data from the analysis.

2.3. CAMS radiation service data

The McClear GHI, BNI, BHI and DHI are freely available through the Atmosphere Data Store of CAMS [12]. The data was downloaded at a temporal resolution of 1 min from the CAMS solar radiation service dataset, where the sky type was selected as cloud-free, which corresponds to McClear values.

The data may also be downloaded in “expert mode”, where the following outputs are provided: clear-sky and all-sky GHI, BNI, BHI and DHI, solar zenith angle, name of vertical profile of atmosphere, total column content in water vapor and ozone, partial aerosol optical depths at 550 nm for black carbon, dust, sea salt, organic matter, sulphate, nitrate, ammonium and secondary organics, surface reflectance parameters, and some cloud information.

2.4. Matching the data under cloud-free skies

This study is only concerned with cloud-free skies, therefore, a new and restrictive cloud-screening algorithm for BSRN radiation observations was applied. The applied cloud-free detection algorithm is based on the correlation between measured GHI and a clear-sky irradiance model (modified Lambert Beer) fitted to measurement over a moving time windows. The core detection criterion applies a threshold on the correlation coefficient between measurements and the fitted model. To address the effects of stochastic signals arising from measurement uncertainty and temporal changes in atmospheric composition, a tolerance parameter is used in the correlation test that depends on the cosine of the solar zenith angle, allowing the detection threshold to dynamically adapt to solar geometry and local atmospheric conditions.

To capture cloud effects occurring at different time scales, a dyadic approach employing multiple moving window lengths (15, 30, 60, and 120 min) is implemented. This multi-scale strategy leverages the complementarity of various temporal resolutions: shorter windows effectively detect brief cloud-induced variations, reducing false negatives at fine time scales, while longer windows improve robustness against transient fluctuations and ensure reliable detection of sustained cloud-free conditions.

Following the selection of cloud-free instances of BSRN data, the quality-assured AERONET data were matched in time to data from their corresponding BSRN stations, such that at each timestamp the maximum absolute time difference between them was no longer than 1-min. The corresponding McClear data was then matched to them at its native 1-min resolution. It is common practice to remove the larger values of the solar zenith angle, e.g., 80°, to avoid horizon obstructions and the directional response of pyranometers. The matching with the AERONET data takes care of that in this study, where the maximum observed solar zenith angle at all stations was 82°.

2.5. Circumsolar irradiance

The circumsolar correction is based on the parametric model of Eissa et al. [25] which estimates the contribution of the circumsolar irradiance to the BNI. The model was developed using libRadtran-derived circumsolar contribution values as a reference. The model coefficients were established from data from two sites, Solar Village in Saudi Arabia and Tamanrasset in Algeria. In practice, the model utilizes the BNI and DHI to classify the sky clearness [33], which is then used for the retrieval of the circumsolar irradiance for any opening half-angle in the interval [0.4°, 5°]. The model takes the form:

$$CSC(\alpha_0,\alpha) = o_1 SC^{\rho_1} + \nu_1, \text{for } SC < 1.92, \tag{4}$$

$$CSC(\alpha_0,\alpha) = o_2 SC^{\rho_2}, \text{for } 1.92 \le SC \le 5.34, \tag{5}$$

$$CSC(\alpha_0,\alpha) = o_3 SC^{\rho_3}, \text{for } SC > 5.34, \tag{6}$$

where CSC is the circumsolar contribution for the defined annular region $[\alpha_0, \alpha]$, where in this case $\alpha_0 = 0.25°$ and α could be any value from 0.4 to 5°. The coefficients (o, ρ, ν) are a function of α and were established using data from the two desert sites combined [25]. The coefficients are available in Table A.3 in the Appendix. SC is a measure of the sky clearness [33], and is computed as:

$$SC = \frac{\frac{(DHI+BNI)}{DHI} + 1.041\theta_S^3}{1 + 1.041\theta_S^3}, \tag{7}$$

where θ_S is expressed in radian, and the BNI and DHI are from McClear.

The CSNI is then computed as:

$$CSNI(\alpha_0,\alpha) \approx \frac{CSC(\alpha_0,\alpha) BNI^{Sun}}{1 - CSC(\alpha_0,\alpha)}, \tag{8}$$

where BNI^{Sun} is the BNI from the solar disc only, in this case considered to be that of McClear. In practice, when using this model the CSNI in the region from 0.25° to the center of the solar disc is considered negligible. In this study, α takes the value of either 2.5° or 2.9° depending on the aperture half-angle of the pyrheliometer of the station under investigation.

Finally, the McClear estimates considering the circumsolar irradiance are computed as:

$$BNI_{\text{modelled}}(\alpha) = BNI_{\text{McClear}} + CSNI_{\text{Eissa_et_al}}(\alpha_0,\alpha), \tag{9}$$

$$DHI_{\text{modelled}}(\alpha) = DHI_{\text{McClear}} - CSHI_{\text{Eissa_et_al}}(\alpha_0,\alpha), \tag{10}$$

$$CSHI = CSNI \cos(\theta_S). \tag{11}$$

Applying this model implies that desert dust aerosol optical properties are assumed to be valid at all locations for the derivation of the circumsolar radiation. In this study the impact of this assumption is assessed in the following section by observing how the correlation coefficient and standard deviation of deviations change when validating the McClear estimates with and without the circumsolar correction. These metrics quantifying the dispersion and correlation between the paired modelled and reference samples provide insight into whether the modelled values are improving or not.

2.6. Performance evaluation protocol

Following the Guide to the expression of uncertainty in measurement [34], the errors between paired samples were computed by subtracting the reference values from the modelled ones, such that a negative value indicates that the measurement is larger than the modelled value, and vice versa. The validations are represented by the statistical measures: RMSE, bias, standard deviation of deviations, and correlation coefficient. Relative values are expressed with respect to the mean reference value of the matched dataset, only daytime values were used as samples with solar zenith angles larger than 82° were filtered.

These metrics were used to evaluate the performance of McClear estimates versus the BSRN measurements, with and without accounting for the circumsolar irradiance. They were also used in the validation of the CAMS AOD versus AERONET data. In addition to these metrics, the scatter density plots used to present the validations showcase the least-squares (LS) affine regression, the first axis of inertia, also known as the first component in principal component analysis (PCA), and the robust affine regression.

When evaluating such performance metrics, one should keep in mind the uncertainties of the radiometers. Normally due to parameters of the sensor such as response time, calibration, cosine response, temperature dependence, aging, zero offsets, parameters of the data acquisition electronics, and parameters controlled by humans such as soiling and leveling [7]. It is difficult to set a precise number when considering such a large network of stations, with different measurement sensors, different weather conditions, and different operation personnel. High-quality operational stations report expanded uncertainties of 3 to 4% for GHI measurements, and 2 to 2.5% for BNI ones [1].

2.7. Data availability

The compiled datasets are entitled ABC-Rad, representing AERONET, BSRN and CAMS Radiation. Following the FAIR principles (Findable, Accessible, Interoperable, and Reusable) [35], and leveraging libinsitu (library of in-situ data) together with a THREDDS server as the hosting platform, the compiled datasets from the 24 stations, along with their associated metadata and attributes, are available for download [36].

3. Results and discussion

To evaluate the applicability of the Eissa et al. model in non-desert environments, and to quantify the impact of the circumsolar irradiance on the McClear BNI and DHI estimates, the validations were performed twice (without and with the circumsolar correction). That was followed by an analysis on the influence of the errors of the CAMS AOD on the McClear estimates.

3.1. Global scale validation of Eissa et al's circumsolar model

For the case of the BNI the validation results are good without and with the CSNI correction. For samples of all stations combined, in relative values, without accounting for the CSNI, the bias is −1.5%, the standard deviation of deviations is 7.4%, the RMSE is 7.5% and the correlation coefficient is 0.946. When including the CSNI all metrics improve to become −0.4%, 7.2%, 7.2% and 0.948, respectively. Although an increase in bias will be observed when adding the CSNI to the BNI, monitoring the standard deviation reveals that the dispersion of the paired samples has improved by 1.7 W m^{-2}. Although this is not a significant improvement, it signifies that the added CSNI is not adding to the dispersion of the paired samples, i.e., it is not just random noise. This then indicates that incorporating the CSNI does lead to an improvement in McClear BNI values. This is further corroborated by the correlation coefficient, which slightly improves from 0.946 to 0.948 when including the CSNI. The validation metrics for each independent station, and all stations combined, are presented in Table A.4 in the appendix.

By observing the stations independently, all stations exhibit an improvement in the standard deviation of deviations and correlation coefficient when accounting for the CSNI. The two stations exhibiting the larger contributions from the CSNI to the BNI are XIA and GOB, which are the two stations with the largest ratio of dust AOD to total AOD. Expectedly as mineral dust AOD is the main aerosol species responsible for the forward scattering of the incoming solar irradiance under cloud-free conditions.

To showcase the improvements, Fig. 2 presents a scatter plot where the *x*-axis depicts the change in standard deviation of deviations (with CSNI correction minus without), as such negative values indicate a smaller dispersion and therefore an improvement. The *y*-axis presents the same for the correlation coefficient, where a positive value is an improvement. The color of each point indicates the ratio of the mean dust AOD to total AOD, and finally the size of each point indicates the mean total AOD of that station. No relationship is evident between the improvements at the 24 stations and either the mean total AOD or the ratio of dust to total AOD.

For the case of DHI, the presented validation results are good for both cases, and when accounting for the circumsolar irradiance the improvement is more pronounced compared to the BNI case. For the samples of all stations combined, without accounting for the CSHI, the bias is 19.0%, the standard deviation of deviations is 26.3%, the RMSE is 32.4% and the correlation coefficient is 0.837. After removing the CSHI from the McClear DHI the metrics improved to become 13.1%, 24.4%, 27.7% and 0.837, respectively.

By observing the stations independently, 22 stations exhibit an improvement in both the standard deviation and correlation coefficient when accounting for the CSHI. LER shows no change in the standard deviation, whereas LER and DAR reveal a slight decrease in the correlation coefficient with the CSHI.

Similar to the analysis of the BNI, Fig. 3 presents the scatter plot showcasing the changes in standard deviation of deviations and correlation coefficient for the DHI case. No distinct relationship between the improvements at the 24 stations and either the mean total AOD or the ratio of dust to total AOD is present. The color coding and point size of the stations exhibit no distinctly visible pattern.

The libRadtran-simulated circumsolar contribution reference values used in the development of the model Eissa et al. were derived from aerosol optical properties collected from two desert sites. The reference computations utilized the AERONET AOD, aerosol single scattering albedo, and aerosol phase function. Consequently, the model implicitly assumes desert type aerosols. Although the samples covered varying conditions, from very clear skies to different dust loadings. Nevertheless, as shown in Figs. 2 and 3, no systematic pattern is observed in the improvements across the 24 stations used in this study.

To ensure that the statistics of all stations combined are not dominated by the few stations with larger sample numbers, station equal statistics were computed by averaging the statistics at each station with equal weights. The results are present in the last rows of Tables A.4 and A.5. Using this method for the BNI the standard deviation of deviations improves by 1.3 W m^{-2} (0.1%) and the correlation coefficient from 0.945 to 0.948, as opposed to the those from all samples combined of 1.7 W m^{-2} (0.2%) and 0.946 to 0.948, respectively. For the DHI the standard deviation of deviations improves by 1.1 W m^{-2} (1.5%) and the correlation coefficient from 0.830 to 0.831, as opposed to the those from all samples combined of 1.5 W m^{-2} (1.9%) and 0.837 to the same 0.837, respectively. These results confirm that conclusions are robust and not dominated by stations with large sample sizes. The minor differences between station equal and sample weighted statistics indicate consistent model performance across all 24 stations.

Therefore, referring to the first research question, the presented results indicate that the circumsolar correction of the Eissa et al. model improves the BNI and DHI retrievals across all sites. This suggests that the approach is applicable to diverse environments for quantifying the circumsolar irradiance.

3.2. Circumsolar irradiance impact on McClear

The first research question has been addressed with a positive outcome. Moving on to the second one, in which the impact of the circumsolar irradiance on the McClear estimates is examined. In this case the focus shifts to changes in McClear DHI and BNI after accounting for the circumsolar irradiance.

Fig. 4 presents the scatter density plot showcasing the validation for all stations combined, along with the relative frequency of the errors of the BNI before and after the CSNI correction. The scatter density plot shows that for the corrected BNI the paired samples are evenly scattered along the identity line, and so are the regions with higher density of samples, which lie on the identity line. On a global scale, when comparing the corrected with the uncorrected BNI metrics of Table A.4, the bias increases by 8.6 W m^{-2}, which in this case corresponds to an improvement from −1.5 to −0.4%, along with slight improvements in the standard deviation (from 7.4 to 7.2%) and RMSE (7.5 to 7.2%). The correlation coefficient also improves from 0.946 to 0.948.

For the DHI, as presented in Fig. 5, the scatter density plot for the corrected DHI shows that the paired samples exhibit a relatively larger scatter along the identity line, and for the larger values the modelled

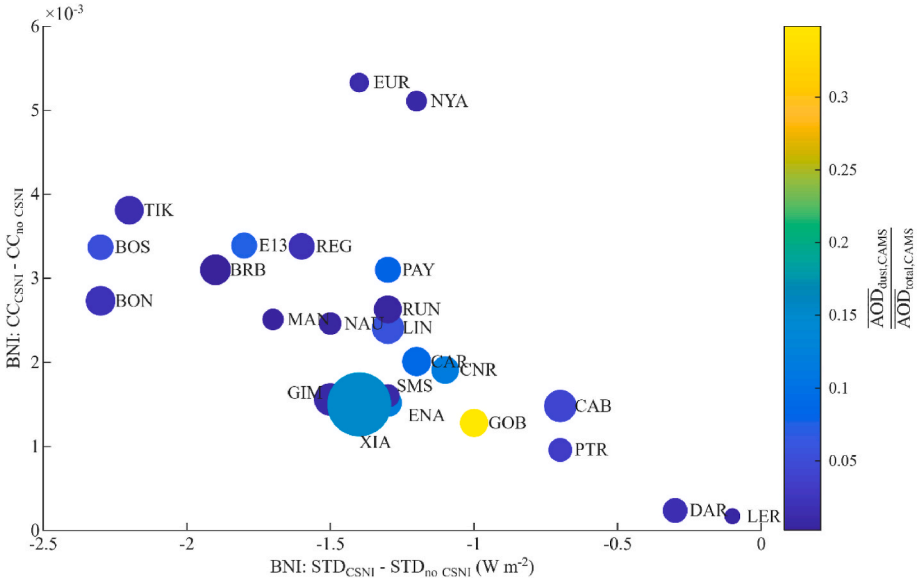


Fig. 2. Scatter plot of the improvements of the standard deviation of deviations (STD) and correlation coefficient (CC) for all 24 stations for the BNI case. The station abbreviation is shown next to its respective point. The color coding is the ratio of the mean dust AOD to mean total AOD, and the size of the point represents the mean total AOD for that station. (For interpretation of the references to color in this figure legend, the reader is referred to the Web version of this article.)

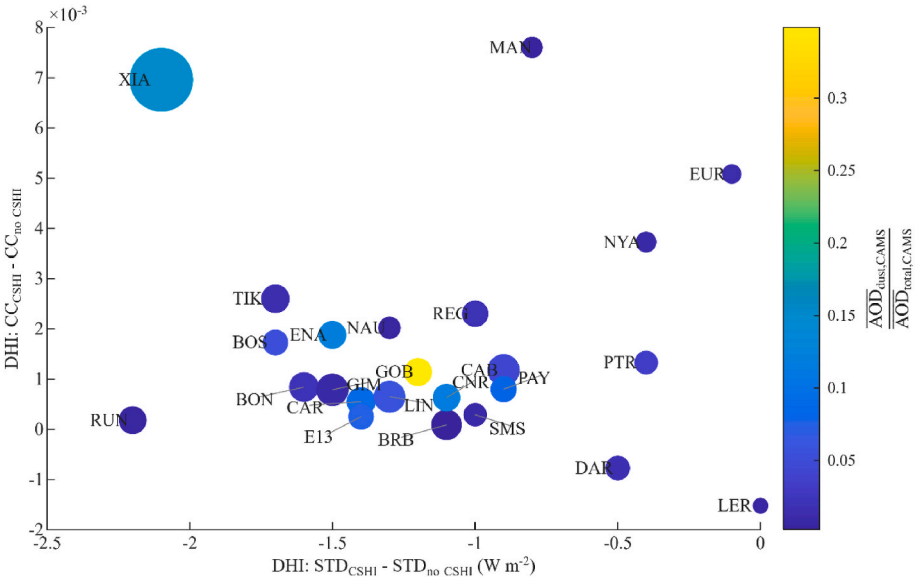


Fig. 3. Scatter plot of the improvements of the standard deviation of deviations (STD) and correlation coefficient (CC) for all 24 stations for the DHI case. The station abbreviation is shown next to its respective point. The color coding is the ratio of the mean dust AOD to mean total AOD, and the size of the point represents the mean total AOD for that station. (For interpretation of the references to color in this figure legend, the reader is referred to the Web version of this article.)

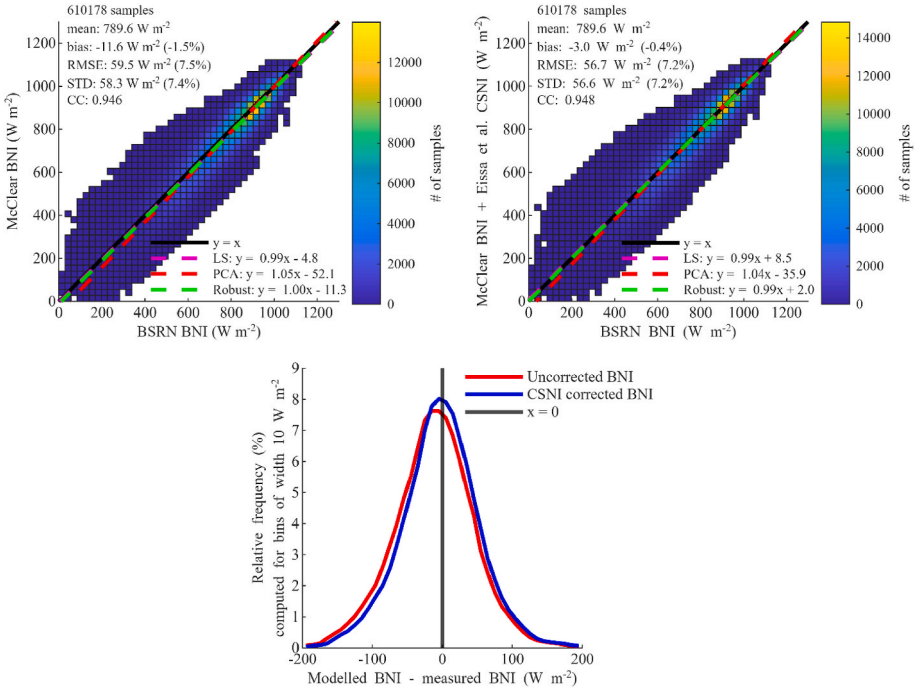


Fig. 4. On the left, the scatter density plot of McClear BNI versus corresponding BSRN reference values is shown, and on the right the same for the CSNI corrected McClear BNI. CC denotes the correlation coefficient, LS the least-squares affine regression, PCA the first component in principal component analysis, and Robust the robust affine regression. On the bottom, the relatively frequency of the errors of the McClear BNI before and after the CSNI correction is shown.

values are underestimated, whereas the opposite is observed for the smaller ones. Compared to the BNI, the relative change due to circumsolar irradiance is more pronounced for the DHI. By observing the corrected and uncorrected metrics of Table A.5, the bias changes by 5.9% (from 19.0 to 13.1%), the standard deviation by 1.9% (from 26.3 to 24.4%), and the RMSE by 4.7% (from 32.4 to 27.7%). The correlation coefficient remains the same at 0.837.

These findings are in line with Elias et al. [26] for cloud-free, but aerosol-loaded conditions, using the SolarRes tool. They report that accounting for the circumsolar irradiance changes (and improves) the bias of the BNI by 1% and by 4% for the DHI, and the RMSE by ~0.5% for both.

To assess the potential impact of bias in *SC* computation on the circumsolar correction, a sensitivity test was conducted. The McClear BNI and DHI were corrected using CSNI and CSHI computed from reference BSRN measurements, to compare to those computed from McClear values. The results revealed that the impact on final corrected irradiance is small. Over all samples for BNI the bias when using BSRN computed CSNI is −0.6% compared to −0.4% when using McClear computed CSNI. For DHI, the bias when using BSRN computed CSHI is 14.6%

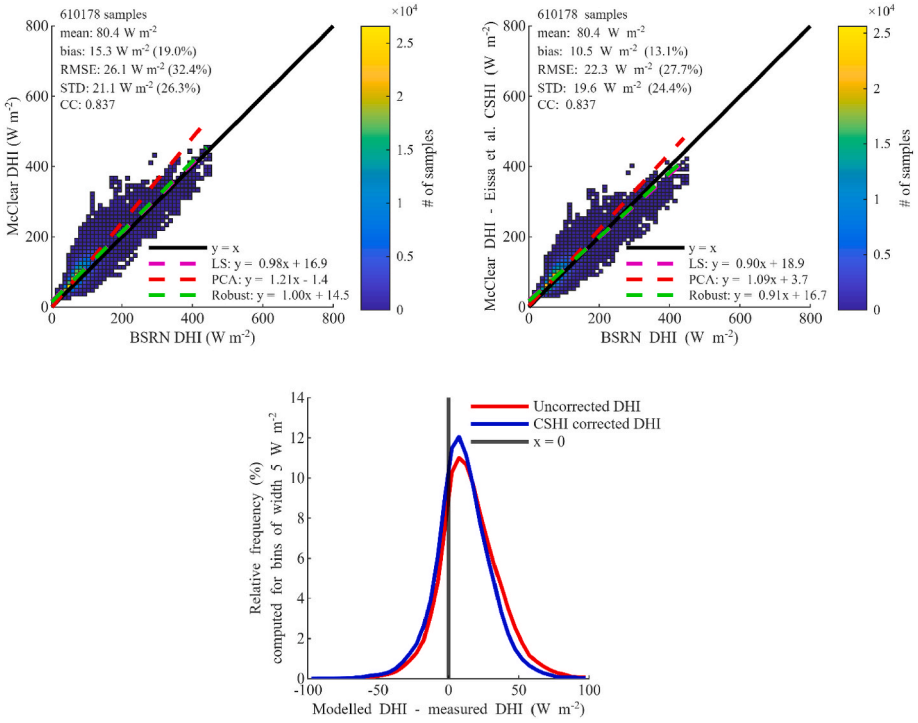


Fig. 5. On the left, the scatter density plot of McClear DHI versus corresponding BSRN reference values is shown, and on the right the same for the CSHI corrected McClear DHI. On the bottom, the relative frequency of the errors of the McClear DHI before and after the CSHI correction is shown.

compared to 13.1% when using McClear computed CSHI. These findings indicate that while the circumsolar correction algorithm exhibits sensitivity to *SC* bias, the final irradiance estimates remain robust to this source of uncertainty.

For completion, the scatter density plot of the GHI validations is presented in Fig. 6, and the GHI validation results of all stations are presented in Table A.6. The paired samples exhibit a small scatter and are well aligned along the identity line, as indicated by the performance metrics which exhibit a bias of 1.3%, standard deviation of 2.9%, RMSE of 3.2%, and a correlation coefficient of 0.998. The plot of the GHI validations is much better when compared to those of the BNI and DHI. This is due to a cancellation of errors when combining the beam and diffuse irradiance.

The circumsolar correction systematically increases the BNI and

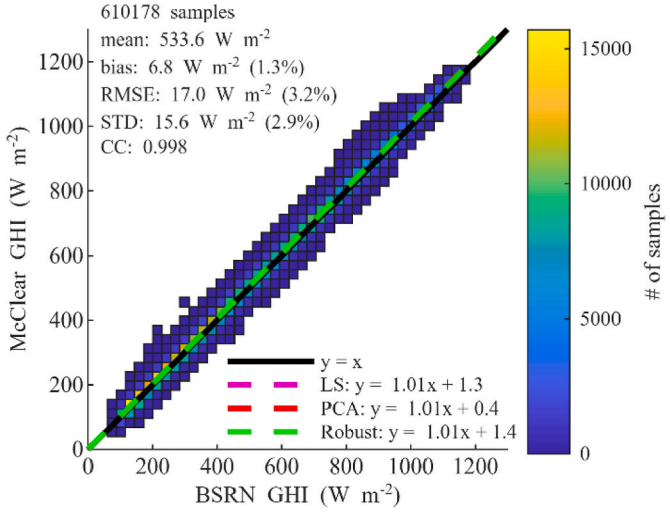


Fig. 6. Scatter density plot of McClear GHI versus corresponding BSRN reference values.

decreases the DHI. This correction is not a simple offset, as demonstrated by observing changes in the standard deviation of deviations and correlation coefficient. The overall change in bias was quantified to be +1% for the BNI and −6% for the DHI. Whether this change is in the favorable direction, i.e., bias moves closer to zero, depends on the bias before the correction. Noting that errors are also strongly dependent on the AOD.

For the BNI samples at all stations combined, as shown in Fig. 4, it is evident that the peak of the curve of the relative frequency of the errors of the CSNI corrected McClear BNI is shifted towards zero, when compared to those of the uncorrected McClear BNI. This is a good sign. For the DHI, a similar pattern is observed where the relative frequency of the errors of the CSHI corrected McClear DHI is more shifted towards zero, when compared to the uncorrected McClear DHI. Examining the bias for each station independently, it is apparent that the improvement in bias is not at all stations (as opposed to improvements in standard deviation and correlation coefficient). The change in bias for the BNI and DHI are presented in Figs. 7 and 8, respectively. The stations are ordered from smallest to largest ratio of mean dust AOD to mean total AOD. For BNI 14 of the 24 stations exhibit a bias closer to zero after the correction, i.e., moving in the right direction. The other 10 stations already had a positive bias before accounting for the CSNI, and as such they will normally be moving further from zero in the positive direction when the CSNI is added. For the DHI the bias of 17 of the 24 stations exhibit an improvement in the bias. Five of the seven remaining stations started with a negative bias before removing the CSHI from the DHI, and as such will normally move further from zero in the negative direction.

Based on the results, it is recommended that cloud-free models incorporate the circumsolar irradiance in their BNI and DHI retrievals, as that will lead to an overall improvement in modelled values, especially when such models are attempting to reproduce such variables as from in situ radiometers. It is also apparent that when accounting for the circumsolar irradiance using the Eissa et al. model neglecting the dominant aerosol species at the different sites is acceptable. The improvements in standard deviation and correlation coefficient observed using the stations of this study show no relation with respect to either the total mean AOD nor the ratio of the mean dust AOD to mean total

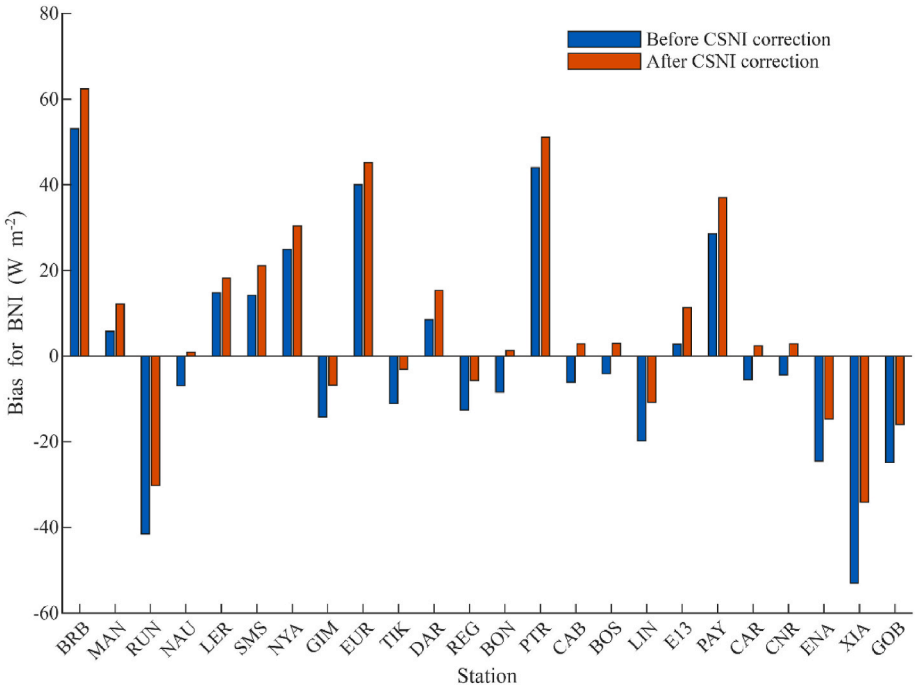


Fig. 7. The bias of the BNI for all stations, with and without accounting for the CSNI.

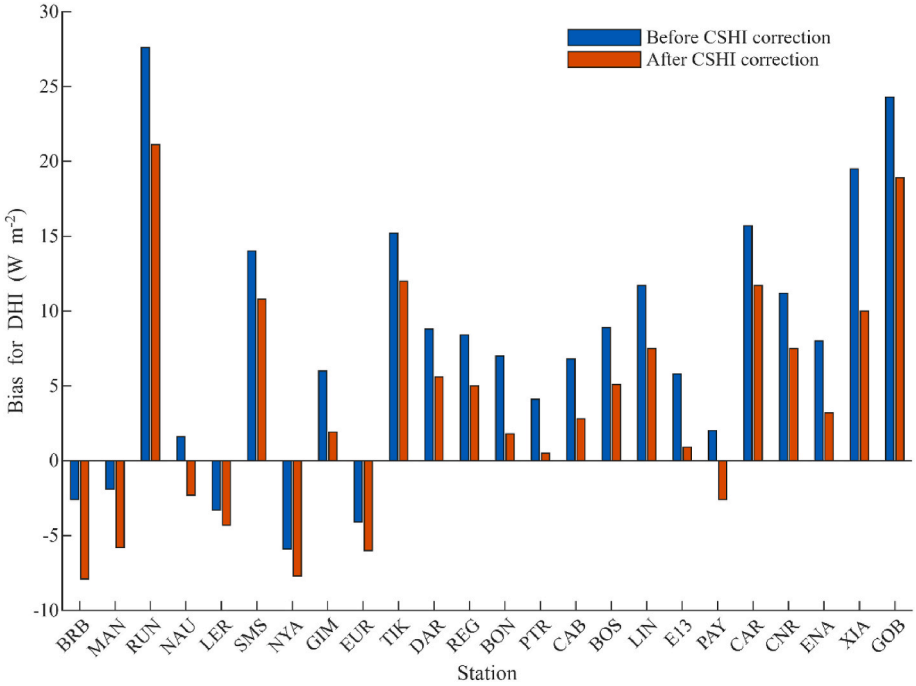


Fig. 8. The bias of the DHI for all stations, with and without accounting for the CSHI.

AOD. Nevertheless, the scatter along the identity line in Figs. 4 and 5 is present after accounting for the circumsolar irradiance. Also, in some stations the bias before accounting for the circumsolar irradiance was already positive for BNI and negative for DHI validations. The sources of which may be attributed to other inputs utilized by McClear.

3.3. CAMS AOD influence on McClear

Having analyzed the circumsolar impacts on McClear, the following continues to analyze the effects of AOD used by McClear on its modelled values.

To demonstrate the influence of the CAMS AOD on the McClear BNI and DHI a comparison is first made between the CAMS AOD and the corresponding reference AOD from AERONET, both at 550 nm. The scatter density plot is shown in Fig. 9 for all stations combined. When compared to the reference value, CAMS AOD exhibits a bias of 15.7%, a standard deviation of deviations of 64.0%, a RMSE of 65.9% and a correlation coefficient of 0.896. To check for station-related dependence for the performance of the CAMS AOD, no dependance is observed in terms of bias and standard deviation with respect to mean AERONET

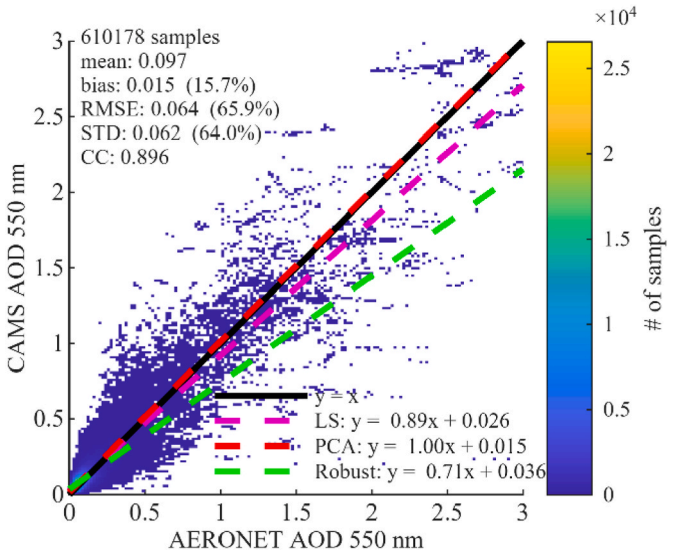


Fig. 9. Scatter density plot of CAMS AOD at 550 nm versus the AERONET reference AOD at 550 nm.

AOD and AERONET Ångström Exponent between 440 and 870 nm (a proxy for aerosol size distribution). This is shown in Fig. 10.

To investigate the bias for different AOD bins, Fig. 11 presents the bias for AERONET AOD bins of 0.1, along with the number of samples available in each bin. The uncertainty of the AERONET AOD taken as reference here is reported between 0.01 and 0.02 [32]. Therefore, the relative higher uncertainty of the AERONET AOD is computed at the center of each bin of Fig. 10 and represented with the dotted line.

The first bin from 0 to 0.1, which comprises the most samples, exhibits a large positive bias of ~40%. This bin is also the one with the largest relative uncertainty of reference values, ~20 to 40% at mid-bin. The large standard deviation of deviations indicates that the errors in paired samples vary more than expected from the reference uncertainty, showing that CAMS AOD tends to overestimate AERONET AOD at smaller values. Subsequent bins exhibit biases near zero, whereas the bins with larger AOD values show negative bias, but the number of samples in these bins is quite small for statistical significance. Indeed, for this dataset only 1% of AERONET samples have an AOD > 0.64, limiting conclusions at high aerosol loads.

Putting this into perspective, it implies that samples where the AOD is overestimated will generally exhibit an underestimation in the beam component and overestimation in the diffuse one, and vice versa. To showcase this effect, the error of the AOD is plotted against the error of the circumsolar corrected McClear BHI, and the same for the circumsolar corrected McClear DHI, respectively in Figs. 12 and 13. The BHI is used in these plots rather than the BNI, as it makes it easier to visualize the effects of the BHI and the DHI on the GHI, eliminating the need for the solar zenith angle. The errors are computed as:

$$\text{error of } BHI = (BHI_{\text{McClear}} + CSHI_{\text{Eissa_et_al}}) - BNI_{\text{BSRN}} \cos(\theta_S), \quad (12)$$

$$\text{error of } DHI = (DHI_{\text{McClear}} - CSHI_{\text{Eissa_et_al}}) - DHI_{\text{BSRN}}, \quad (13)$$

$$\text{error of } GHI = GHI_{\text{McClear}} - GHI_{\text{BSRN}}, \quad (14)$$

$$\text{error of } AOD = \text{AOD}_{\text{CAMS}} - AOD_{\text{AERONET}}. \quad (15)$$

It is evident that the errors of the BHI and DHI are highly correlated with the errors of the AOD. Noting that this comparison is using the AOD at 550 nm, whereas the irradiance is broadband. The higher dispersion in Fig. 13 may also be attributed to other variables such as the Ångström Exponent, absorption Ångström Exponent, aerosol single scattering albedo and phase function. Nevertheless, the strong correlation between AOD errors and irradiance deviations indicates that AOD is likely a significant driver of remaining McClear uncertainties, though other factors may also contribute.

Referring to the last question of this study regarding the influence of the CAMS AOD on the performance of McClear, it is evident that it is non-negligible. The dependence of CAMS AOD on BNI accuracy is further corroborated by Salamalikis et al. [20], who showed that a pre-calibration of the CAMS AOD led to improved metrics for BNI retrieval using a radiative transfer model. Therefore, more accurate modelling of the CAMS AOD will in turn improve the McClear irradiance estimates, which will in turn improve the CAMS Radiation Service. To further investigate the exact effects, as a further study, the McClear model may be operated twice for comparison purposes. Once using the CAMS AOD and the other using the AERONET AOD.

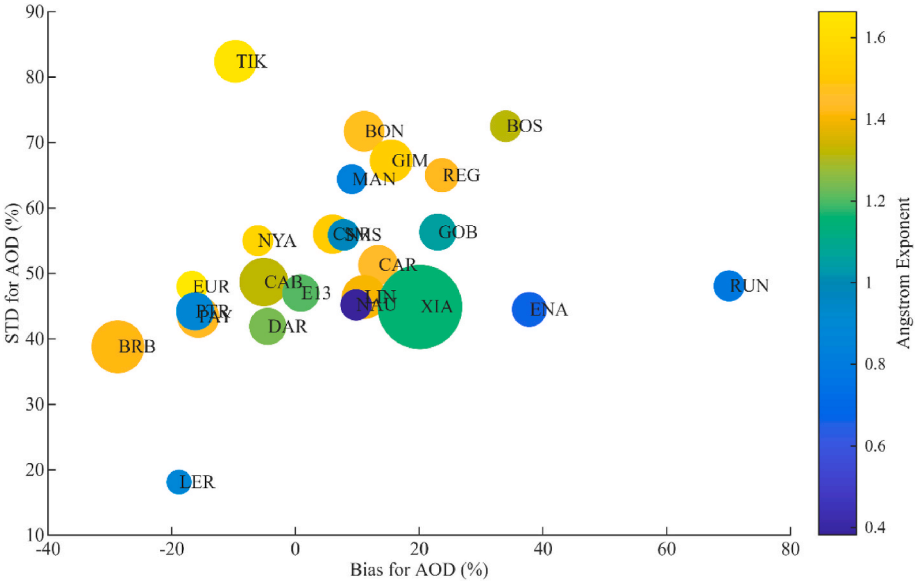


Fig. 10. CAMS versus AERONET AOD for all 24 stations, in terms of bias on *x*-axis, standard deviation on *y*-axis, color-coded Ångström Exponent. The mean AERONET AOD at each station is represented by the size of the circle. (For interpretation of the references to color in this figure legend, the reader is referred to the Web version of this article.)

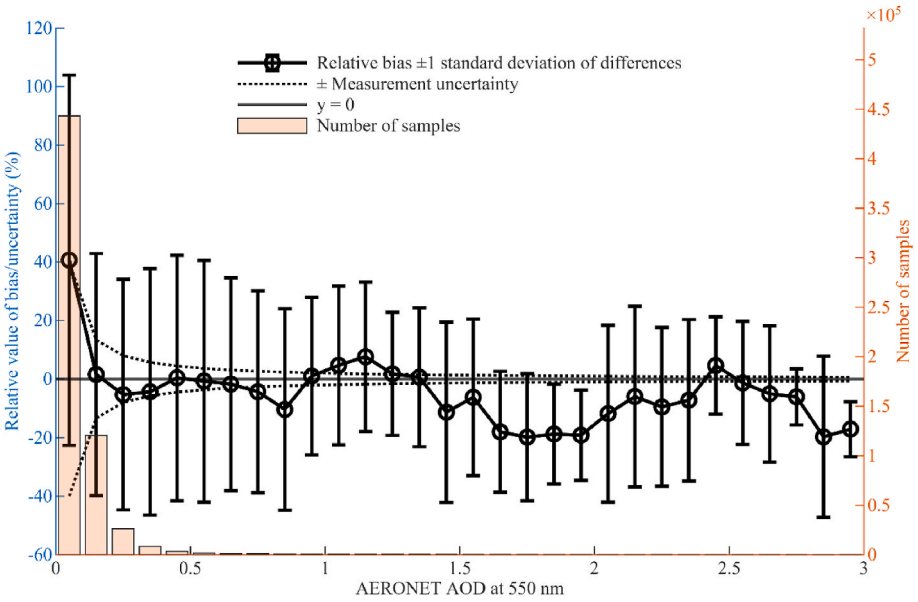


Fig. 11. The relative bias of the CAMS AOD at bins having widths of 0.1 of the AERONET AOD. For each bin, the standard deviation of difference is also shown, along with the relative uncertainty of the reference AERONET AOD. The number of samples within each bin is also shown.

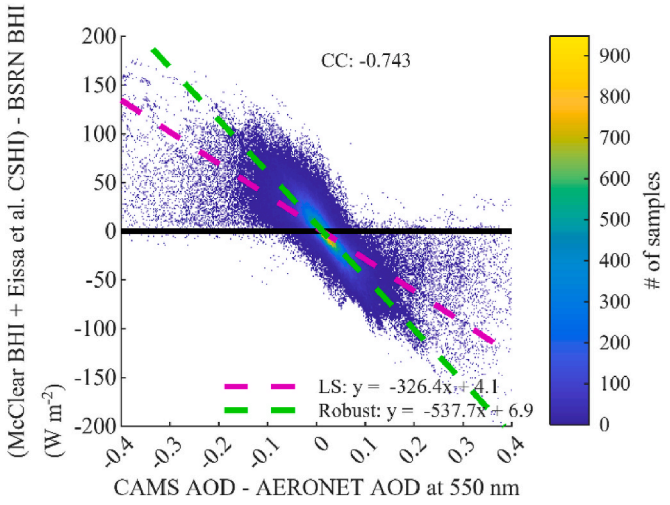


Fig. 12. Scatter density plot of errors of circumsolar corrected BHI versus errors of AOD.

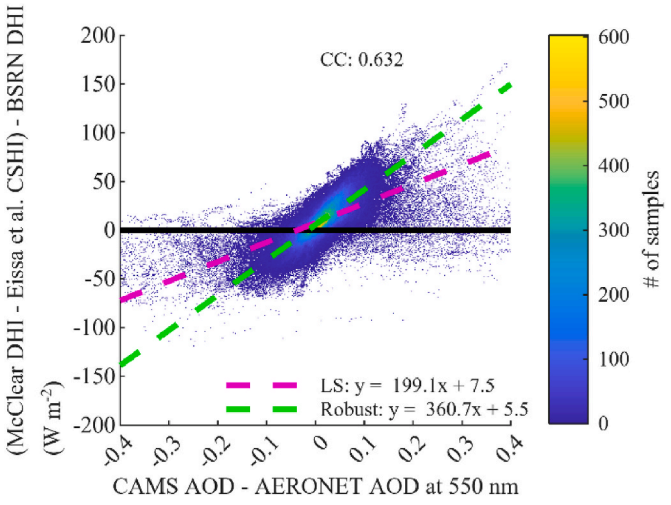


Fig. 13. Scatter density plot of errors of circumsolar corrected DHI versus errors of AOD.

Errors of the McClear GHI are substantially smaller due to BHI and DHI errors compensating for one another, as shown in Fig. 14, which supports the very good validations of the GHI presented in Fig. 6 and Table A.6.

4. Conclusion and prospects

With respect to the McClear estimates of the CAMS Radiation Service, and a potential operational implementation of a method extension, the effects of circumsolar irradiance and aerosol optical depth on beam and diffuse irradiance were analyzed globally. Applying the circumsolar correction of Eissa et al. improved McClear retrievals at all stations. This global scale validation suggests the applicability of the model extends beyond the desert type aerosol for which it was originally developed. This finding is in line with Elias et al., where they concluded that neglecting aerosol type in the computation of the circumsolar component is acceptable. For the CSNI corrected BNI, the standard deviation of deviations improved by 0.2%, RMSE by 0.3%, correlation coefficient from 0.946 to 0.948, and bias shifted from −1.5% to −0.4%. The improvements were more pronounced for DHI: standard deviation improved by 1.9%, RMSE by 4.7%, and bias decreased from +19.0% to +13.1%. These results support a potential simplified operational implementation in the CAMS Radiation Service.

Despite the circumsolar correction, remaining deviations between McClear and BSRN measurements are strongly correlated with errors in the CAMS modelled AOD. This suggests that the AOD is a major driver whose uncertainty affects both the bias and scatter in modelled beam and diffuse irradiance. The current CAMS AOD exhibits high scatter (standard deviation of 64.0%) and an overall positive bias of 15.7%. The CAMS AOD continues to evolve through successive cycles. Therefore, further studies may investigate the accuracy of the CAMS AOD at different wavelengths and different cycles, along with their effects on the solar irradiance.

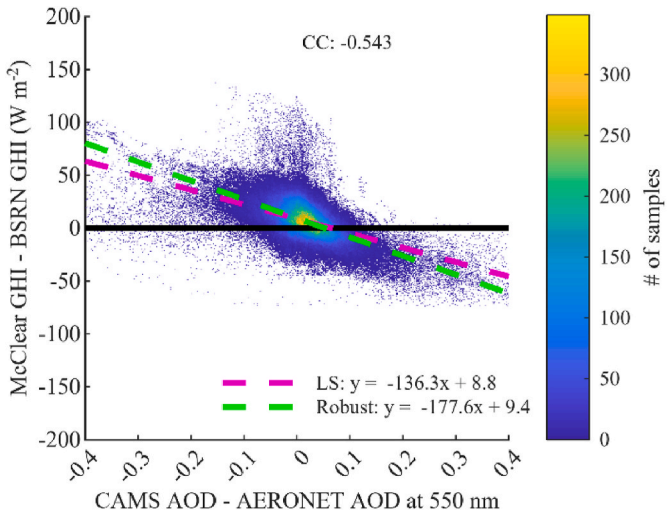


Fig. 14. Scatter density plot of errors of GHI versus errors of AOD.

CRediT authorship contribution statement

Yehia Eissa: Writing – review & editing, Writing – original draft, Visualization, Validation, Methodology, Formal analysis, Data curation, Conceptualization. **Yves-Marie Saint-Drenan:** Writing – review & editing, Visualization, Validation, Software, Methodology, Formal analysis, Data curation, Conceptualization. **Marion Schroedter-Homscheidt:** Writing – review & editing, Visualization, Validation, Methodology, Formal analysis. **Antti Arola:** Writing – review & editing, Validation, Formal analysis. **Philippe Blanc:** Writing – review & editing, Supervision, Methodology, Conceptualization.

Data statement

The compiled datasets are entitled ABC-Rad, representing AERONET, BSRN and CAMS Radiation. Following the FAIR principles (Findable, Accessible, Interoperable, and Reusable) [35], and leveraging libinsitu (library of in-situ data; http://libinsitu.org/) together with a THREDDS server as the hosting platform (https://tds.webservice-energy.org/thredds/catalog/catalog.html), the compiled datasets from the 24 stations, along with their associated metadata and attributes, are available for download [36].

Declaration of competing interest

The authors declare that they have no known competing financial interests or personal relationships that could have appeared to influence the work reported in this paper.

Acknowledgements

The research leading to these results has received funding from SciDoSol, a sponsorship chair at Mines Paris – PSL funded by TotalEnergies, RTE, Somfy, TSE and CalibSun. And from the Copernicus Atmosphere Monitoring Service, a program being operated by the European Centre for Medium-Range Weather Forecasts (ECMWF) on behalf of the European Union. It also took place within the Task 16 "Solar Resource for High Penetration and Large Scale Applications" of the Photovoltaic Power Systems Programme (PVPS) of the International Energy Agency (IEA). The authors also thank the PIs of AERONET and BSRN stations, along with all the personnel who installed and maintained the instruments.

Appendix A

Tables A.1 and A.2 present the validations for McClear global and beam irradiance from several studies, summarized by the RMSE, bias, their relative values normalized by the mean reference values, and the correlation coefficient. Table A.3 presents the coefficients of the Eissa et al. model. Tables A.4 and A.5 present the performance evaluation metrics for the validations of the McClear BNI and the DHI for the two cases, with and without the circumsolar irradiance. Table A.6 presents the metrics for the validations of the GHI. Stations are listed in ascending order by their dust contribution to the total aerosol optical depth.

Table A.1
Validations of McClear estimated GHI from several scientific articles from the literature. Regions are presented as: Africa (AF), Asia (AS), Europe (EU), Middle East and Northern Africa (MENA), North American (NA), Oceania (OC), and South and Central America (SA).

Reference	Time step	GHI		
		RMSE	bias	CC
[37]: 9 stations in EU, MENA, NA.	1 min	[19, 38] W m^{-2} [4, 6] %	[2, 13] W m^{-2} [0, 2] %	> 0.990
[18]: 21 stations in AF, EU, MENA.	1 h	[14, 58] W m^{-2} [2, 11] %	[−9, 53] W m^{-2} [−2, 10] %	Not reported
[13]: 11 BSRN stations in AS, EU, MENA, NA, OC, SA.	1 min	[21, 38] W m^{-2} [3, 6] %	[−16, 17] W m^{-2} [−3, 3] %	[0.982, 0.999]
[38]: 13 stations in South Africa.	1 min	[13, 45] W m^{-2} [3, 9] %	[−38, 24] W m^{-2} [−8, 5] %	[0.994, 0.999]

Table A.2
Validations of McClear estimated beam irradiance (BNI or BHI) from several scientific articles from the literature. Regions are presented as: Africa (AF), Asia (AS), Europe (EU), Middle East and Northern Africa (MENA), North American (NA), Oceania (OC), and South and Central America (SA).

Reference	Time step	BNI/BHI		
		RMSE	Bias	CC

(*continued on next page*)

Table A.2 (*continued*)

Reference	Time step	BNI/BHI		
		RMSE	Bias	CC
[37]: 9 stations in EU, MENA, NA.	1 min	[23, 82] W m^{-2} [8, 16] %	[−51, 16] W m^{-2} [−10, 3] %	> 0.949
[18]: 21 stations in AF, EU, MENA.	1 h	[46, 91] W m^{-2} [6, 12] %	[−72, 65] W m^{-2} [−8, 9] %	Not reported
[13]: 11 BSRN stations in AS, EU, MENA, NA, OC, SA.	1 min	[32, 71] W m^{-2} [5, 11] %	[−53, 27] W m^{-2} [−8, 5] %	[0.911, 0.996]

Table A.3

The coefficients of the model of Eissa et al. coefficients (o, ρ, ν) are a function of α and each is computed using a 6th order polynomial as: $f(\alpha) = \sum_{j=0}^{6} c_j \alpha^j$, where α is in units of degree. The values of c_j for o, ρ and ν are listed for the version of the model developed using the data from the Solar Village and Tamanrasset.

$f(\alpha)$	c_6	c_5	c_4	c_3	c_2	c_1	c_0
o_1	-4.276×10^{-5}	4.495×10^{-4}	6.590×10^{-4}	-2.574×10^{-2}	1.073×10^{-1}	-1.815×10^{-2}	-3.474×10^{-3}
ρ_1	2.014×10^{-3}	-3.441×10^{-2}	2.303×10^{-1}	-7.637×10^{-1}	1.297	-6.506×10^{-1}	−5.514
ν_1	-9.722×10^{-6}	1.318×10^{-4}	-4.334×10^{-4}	-1.780×10^{-3}	1.364×10^{-2}	-1.289×10^{-3}	-8.128×10^{-4}
o_2	-1.915×10^{-5}	2.791×10^{-4}	-9.534×10^{-4}	-5.358×10^{-3}	4.534×10^{-2}	-8.467×10^{-3}	-1.263×10^{-3}
ρ_2	-4.632×10^{-5}	9.383×10^{-4}	-7.707×10^{-3}	3.192×10^{-2}	-6.051×10^{-2}	1.006×10^{-2}	−1.577
o_3	-8.189×10^{-5}	1.221×10^{-3}	-4.916×10^{-3}	-1.381×10^{-2}	1.516×10^{-1}	-3.477×10^{-2}	-2.082×10^{-3}
ρ_3	-1.584×10^{-4}	2.870×10^{-3}	-2.056×10^{-2}	7.276×10^{-2}	-1.198×10^{-1}	3.107×10^{-2}	−2.281

Table A.4

BNI validation results of 1 min samples, with and without accounting for the CSNI. Stations are sorted from smallest to largest ratio of mean dust AOD versus mean total AOD as modelled by the CAMS IFS-COMPO.

BSRN Abbreviation	Mean reference value (W m^{-2})	Bias in W m^{-2} (%)		Standard deviation in W m^{-2} (%)		RMSE in W m^{-2} (%)		Correlation Coefficient	
		Without CSNI	With CSNI	Without CSNI	With CSNI	Without CSNI	With CSNI	Without CSNI	With CSNI
BRB	710.0	53.1 (7.5%)	62.4 (8.8%)	63.2 (8.9%)	61.3 (8.6%)	82.5 (11.6%)	87.5 (12.3%)	0.932	0.935
MAN	821.2	5.8 (0.7%)	12.2 (1.5%)	37.7 (4.6%)	36.0 (4.4%)	38.2 (4.6%)	38.0 (4.6%)	0.964	0.966
RUN	800.7	−41.5 (−5.2%)	−30.2 (−3.8%)	37.6 (4.7%)	36.3 (4.5%)	56.1 (7.0%)	47.2 (5.9%)	0.965	0.968
NAU	751.1	−6.9 (−0.9%)	0.9 (0.1%)	42.4 (5.6%)	40.9 (5.4%)	42.9 (5.7%)	40.9 (5.4%)	0.960	0.962
LER	754.1	14.8 (2.0%)	18.2 (2.4%)	11.5 (1.5%)	11.4 (1.5%)	18.7 (2.5%)	21.4 (2.8%)	0.993	0.993
SMS	761.6	14.2 (1.9%)	21.1 (2.8%)	47.7 (6.3%)	46.4 (6.1%)	49.7 (6.5%)	51.0 (6.7%)	0.959	0.961
NYA	714.5	24.9 (3.5%)	30.4 (4.3%)	57.6 (8.1%)	56.4 (7.9%)	62.8 (8.8%)	64.0 (9.0%)	0.873	0.878
GIM	765.5	−14.2 (−1.9%)	−6.8 (−0.9%)	52.9 (6.9%)	51.4 (6.7%)	54.7 (7.1%)	51.9 (6.8%)	0.954	0.956
EUR	719.4	40.0 (5.6%)	45.2 (6.3%)	44.0 (6.1%)	42.6 (5.9%)	59.5 (8.3%)	62.1 (8.6%)	0.911	0.916
TIK	677.5	−11.1 (−1.6%)	−3.1 (−0.5%)	68.0 (10.0%)	65.8 (9.7%)	68.8 (10.2%)	65.9 (9.7%)	0.929	0.933
DAR	709.8	8.5 (1.2%)	15.3 (2.1%)	40.2 (5.7%)	39.9 (5.6%)	41.1 (5.8%)	42.7 (6.0%)	0.965	0.965
REG	793.5	−12.6 (−1.6%)	−5.7 (−0.7%)	62.2 (7.8%)	60.6 (7.6%)	63.5 (8.0%)	60.9 (7.7%)	0.922	0.925
BON	784.8	−8.4 (−1.1%)	1.3 (0.2%)	49.4 (6.3%)	47.1 (6.0%)	50.1 (6.4%)	47.1 (6.0%)	0.957	0.960
PTR	728.7	44.0 (6.0%)	51.1 (7.0%)	46.4 (6.4%)	45.7 (6.3%)	63.9 (8.8%)	68.5 (9.4%)	0.959	0.960
CAB	652.4	−6.1 (−0.9%)	2.9 (0.4%)	64.2 (9.8%)	63.5 (9.7%)	64.5 (9.9%)	63.6 (9.7%)	0.933	0.934
BOS	867.0	−4.1 (−0.5%)	3.0 (0.3%)	53.9 (6.2%)	51.6 (6.0%)	54.0 (6.2%)	51.7 (6.0%)	0.939	0.942
LIN	709.0	−19.8 (−2.8%)	−10.8 (−1.5%)	60.1 (8.5%)	58.8 (8.3%)	63.3 (8.9%)	59.7 (8.4%)	0.939	0.941
E13	814.5	2.8 (0.3%)	11.3 (1.4%)	47.0 (5.8%)	45.2 (5.5%)	47.1 (5.8%)	46.6 (5.7%)	0.951	0.955
PAY	766.2	28.5 (3.7%)	37.0 (4.8%)	56.9 (7.4%)	55.6 (7.3%)	63.7 (8.3%)	66.8 (8.7%)	0.931	0.934
CAR	737.8	−5.5 (−0.7%)	2.4 (0.3%)	57.0 (7.7%)	55.8 (7.6%)	57.2 (7.8%)	55.9 (7.6%)	0.940	0.942
CNR	745.4	−4.4 (−0.6%)	2.9 (0.4%)	57.0 (7.6%)	55.9 (7.5%)	57.1 (7.7%)	55.9 (7.5%)	0.941	0.943
ENA	724.5	−24.5 (−3.4%)	−14.7 (−2.0%)	42.1 (5.8%)	40.8 (5.6%)	48.7 (6.7%)	43.4 (6.0%)	0.972	0.974
XIA	550.0	−53.0 (−9.6%)	−34.1 (−6.2%)	83.6 (15.2%)	82.2 (14.9%)	99.0 (18.0%)	89.0 (16.2%)	0.950	0.951

(*continued on next page*)

Table A.4 (*continued*)

BSRN Abbreviation	Mean reference value (W m^{-2})	Bias in W m^{-2} (%)		Standard deviation in W m^{-2} (%)		RMSE in W m^{-2} (%)		Correlation Coefficient	
		Without CSNI	With CSNI	Without CSNI	With CSNI	Without CSNI	With CSNI	Without CSNI	With CSNI
GOB	845.4	−24.8 (−2.9%)	−16.0 (−1.9%)	52.1 (6.2%)	51.1 (6.0%)	57.7 (6.8%)	53.5 (6.3%)	0.947	0.949
All data combined	789.6	−11.6 (−1.5%)	−3.0 (−0.4%)	58.3 (7.4%)	56.6 (7.2%)	59.5 (7.5%)	56.7 (7.2%)	0.946	0.948
Equal station weights	746.0	0.0 (−0.1%)	8.2 (1.1%)	51.4 (7.0%)	50.1 (6.9%)	56.9 (7.8%)	55.6 (7.6%)	0.945	0.948

Table A.5
DHI validation results of 1 min samples, with and without accounting for the CSHI. Stations are sorted from smallest to largest ratio of mean dust AOD versus mean total AOD as modelled by the CAMS IFS-COMPO.

BSRN Abbreviation	Mean reference value (W m^{-2})	Bias in W m^{-2} (%)		Standard deviation in W m^{-2} (%)		RMSE in W m^{-2} (%)		Correlation Coefficient	
		Without CSHI	With CSHI	Without CSHI	With CSHI	Without CSHI	With CSHI	Without CSHI	With CSHI
BRB	95.6	−2.6 (−2.8%)	−7.9 (−8.2%)	18.1 (18.9%)	17.0 (17.8%)	18.3 (19.1%)	18.7 (19.6%)	0.863	0.863
MAN	81.8	−1.9 (−2.4%)	−5.8 (−7.1%)	16.3 (20.0%)	15.5 (19.0%)	16.4 (20.1%)	16.6 (20.2%)	0.736	0.743
RUN	76.2	27.6 (36.2%)	21.1 (27.7%)	17.4 (22.8%)	15.2 (19.9%)	32.6 (42.8%)	26.0 (34.2%)	0.831	0.831
NAU	76.4	1.6 (2.1%)	−2.3 (−3.0%)	15.9 (20.8%)	14.6 (19.1%)	15.9 (20.9%)	14.8 (19.3%)	0.758	0.760
LER	53.5	−3.3 (−6.2%)	−4.3 (−8.1%)	4.2 (7.8%)	4.2 (7.8%)	5.3 (9.9%)	6.0 (11.2%)	0.797	0.796
SMS	58.1	14.0 (24.1%)	10.8 (18.6%)	11.6 (20.0%)	10.6 (18.2%)	18.2 (31.3%)	15.1 (26.0%)	0.873	0.873
NYA	61.7	−5.9 (−9.5%)	−7.7 (−12.4%)	10.8 (17.5%)	10.4 (16.8%)	12.3 (19.9%)	12.9 (20.9%)	0.723	0.727
GIM	83.2	6.0 (7.2%)	1.9 (2.3%)	18.8 (22.6%)	17.3 (20.8%)	19.7 (23.7%)	17.4 (20.9%)	0.884	0.885
EUR	60.1	−4.1 (−6.8%)	−6.0 (−9.9%)	12.8 (21.4%)	12.7 (21.1%)	13.5 (22.4%)	14.0 (23.3%)	0.703	0.708
TIK	54.5	15.2 (27.9%)	12.0 (22.1%)	15.3 (28.1%)	13.6 (24.9%)	21.6 (39.6%)	18.1 (33.2%)	0.884	0.887
DAR	69.9	8.8 (12.6%)	5.6 (8.0%)	9.0 (12.9%)	8.5 (12.2%)	12.6 (18.1%)	10.2 (14.6%)	0.884	0.884
REG	73.3	8.4 (11.5%)	5.0 (6.9%)	19.7 (26.9%)	18.7 (25.5%)	21.5 (29.3%)	19.3 (26.4%)	0.740	0.743
BON	84.4	7.0 (8.2%)	1.8 (2.2%)	17.1 (20.3%)	15.5 (18.3%)	18.5 (21.9%)	15.6 (18.4%)	0.889	0.889
PTR	73.6	4.1 (5.6%)	0.5 (0.6%)	13.4 (18.2%)	13.0 (17.6%)	14.0 (19.1%)	13.0 (17.6%)	0.853	0.854
CAB	82.9	6.8 (8.2%)	2.8 (3.3%)	17.3 (20.8%)	16.4 (19.7%)	18.5 (22.4%)	16.6 (20.0%)	0.864	0.866
BOS	69.8	8.9 (12.7%)	5.1 (7.3%)	17.8 (25.4%)	16.1 (23.0%)	19.9 (28.4%)	16.9 (24.1%)	0.829	0.831
LIN	80.2	11.7 (14.5%)	7.5 (9.3%)	17.1 (21.3%)	15.8 (19.7%)	20.7 (25.8%)	17.4 (21.7%)	0.870	0.870
E13	82.8	5.8 (7.1%)	0.9 (1.1%)	17.5 (21.1%)	16.1 (19.4%)	18.4 (22.3%)	16.1 (19.4%)	0.842	0.842
PAY	83.0	2.0 (2.4%)	−2.6 (−3.1%)	18.0 (21.7%)	17.1 (20.6%)	18.1 (21.8%)	17.3 (20.8%)	0.807	0.808
CAR	73.4	15.7 (21.4%)	11.7 (15.9%)	17.9 (24.4%)	16.5 (22.5%)	23.8 (32.4%)	20.2 (27.5%)	0.857	0.858
CNR	73.8	11.2 (15.2%)	7.5 (10.2%)	17.5 (23.6%)	16.4 (22.2%)	20.7 (28.1%)	18.1 (24.4%)	0.855	0.856
ENA	80.0	8.0 (10.0%)	3.2 (3.9%)	15.3 (19.2%)	13.8 (17.2%)	17.3 (21.6%)	14.1 (17.7%)	0.868	0.869
XIA	127.5	19.5 (15.3%)	10.0 (7.9%)	30.6 (24.0%)	28.5 (22.4%)	36.3 (28.5%)	30.2 (23.7%)	0.897	0.904
GOB	84.5	24.3 (28.7%)	18.9 (22.4%)	20.4 (24.1%)	19.2 (22.7%)	31.7 (37.5%)	26.9 (31.9%)	0.806	0.807
All data combined	80.4	15.3 (19.0%)	10.5 (13.1%)	21.1 (26.3%)	19.6 (24.4%)	26.1 (32.4%)	22.3 (27.7%)	0.837	0.837
Equal station weights	76.7	7.9 (10.5%)	3.7 (5.2%)	16.2 (21.2%)	15.1 (19.7%)	19.4 (25.6%)	17.1 (22.6%)	0.830	0.831

Table A.6
GHI validation results of 1 min samples. Stations are sorted from smallest to largest ratio of mean dust AOD versus mean total AOD as modelled by the CAMS IFS-COMPO.

BSRN Abbreviation	Mean reference value (W m^{-2})	Bias in W m^{-2} (%)	Standard deviation in W m^{-2} (%)	RMSE in W m^{-2} (%)	Correlation Coefficient
BRB	526.8	24.0 (4.5%)	17.3 (3.3%)	29.6 (5.6%)	0.998
MAN	631.7	2.8 (0.4%)	15.0 (2.4%)	15.3 (2.4%)	0.999
RUN	559.5	2.2 (0.4%)	10.1 (1.8%)	10.3 (1.8%)	0.999
NAU	484.4	7.6 (1.6%)	12.9 (2.7%)	14.9 (3.1%)	0.999
LER	304.9	−12.1 (−4.0%)	2.9 (0.9%)	12.4 (4.1%)	0.999
SMS	452.5	5.2 (1.1%)	10.9 (2.4%)	12.1 (2.7%)	0.999
NYA	299.1	−5.4 (−1.8%)	7.5 (2.5%)	9.3 (3.1%)	0.998
GIM	514.1	−4.2 (−0.8%)	12.6 (2.5%)	13.3 (2.6%)	0.999
EUR	328	−3.2 (−1.0%)	10.6 (3.2%)	11.1 (3.4%)	0.996
TIK	331.9	−7.2 (−2.2%)	12.7 (3.8%)	14.6 (4.4%)	0.998
DAR	441.1	22.2 (5.0%)	11.5 (2.6%)	25.0 (5.7%)	0.999
REG	472	−6.5 (−1.4%)	12.9 (2.7%)	14.4 (3.1%)	0.998
BON	495.2	9.6 (1.9%)	14.3 (2.9%)	17.2 (3.5%)	0.999
PTR	493.6	35.2 (7.1%)	28.4 (5.8%)	45.3 (9.2%)	0.998
CAB	379.7	3.4 (0.9%)	11.1 (2.9%)	11.6 (3.1%)	0.999
BOS	529.1	11.1 (2.1%)	15.8 (3.0%)	19.3 (3.6%)	0.998
LIN	419.4	1.7 (0.4%)	10.7 (2.5%)	10.8 (2.6%)	0.999
E13	534.9	17.3 (3.2%)	15.9 (3.0%)	23.5 (4.4%)	0.998
PAY	503.2	14.9 (3.0%)	11.1 (2.2%)	18.6 (3.7%)	0.999
CAR	458.8	13.8 (3.0%)	14.1 (3.1%)	19.7 (4.3%)	0.999
CNR	460.2	8.2 (1.8%)	12.4 (2.7%)	14.8 (3.2%)	0.999
ENA	458	10.0 (2.2%)	14.6 (3.2%)	17.7 (3.9%)	0.999
XIA	424.2	−14.8 (−3.5%)	20.8 (4.9%)	25.5 (6.0%)	0.996
GOB	639.8	7.2 (1.1%)	12.9 (2.0%)	14.7 (2.3%)	0.999
All data combined	533.6	6.8 (1.3%)	15.6 (2.9%)	17.0 (3.2%)	0.998

References

[1] M. Sengupta, A. Habte, S. Wilbert, C.A. Gueymard, J. Remund, E. Lorenz, W. van Sark, A.R. Jensen, in: Best Practices Handbook for the Collection and Use of Solar Resource Data for Solar Energy Applications, fourth ed., National Renewable Energy Laboratory, Golden, CO, 2024. NREL/TP-5D00-88300, https://www.nrel.gov/docs/fy24osti/88300.pdf. (Accessed 24 January 2025).

[2] T. Ranchin, M. Trolliet, L. Ménard, L. Wald, Which variables are essential for renewable energies? Int. J. Digit. Earth 13 (2020) 253–261, https://doi.org/10.1080/17538947.2019.1679267.

[3] H.U. Heinrichs, J.M. Weinand, S. Kebrich, J.C. Gómez Trillos, S. Chen, M. Hoffmann, T. Tsani, R. Chen, W. Hu, J. Schmidt, C. Ulbrich, V. Mikhnych, J. Linßen, R. McKenna, Large-scale resource assessments for solar photovoltaics: a review of potential definitions, methodologies and future research needs, Renew. Energy 261 (2026), https://doi.org/10.1016/j.renene.2025.125080.

[4] P. Blanc, B. Espinar, N. Geuder, C. Gueymard, R. Meyer, R. Pitz-Paal, B. Reinhardt, D. Renné, M. Sengupta, L. Wald, S. Wilbert, Direct normal irradiance related definitions and applications: the circumsolar issue, Sol. Energy 110 (2014) 561–577, https://doi.org/10.1016/j.solener.2014.10.001.

[5] S. Wilbert, B. Reinhardt, J. DeVore, M. Röger, R. Pitz-Paal, C. Gueymard, R. Buras, Measurement of solar radiance profiles with the Sun and Aureole Measurement system, J. Sol. Energy Eng. 135 (2013) 041002, https://doi.org/10.1115/1.4024244.

[6] J.A. Ruiz-Arias, SPARTA: solar parameterization for the radiative transfer of the cloudless atmosphere, Renew. Sustain. Energy Rev. 188 (2023) 113833, https://doi.org/10.1016/j.rser.2023.113833.

[7] WMO, Guide to Instruments and Methods of Observation: Volume I – Measurement of Meteorological Variables, 2024, https://doi.org/10.59327/WMO/CIMO/1.

[8] Y. Xie, M. Sengupta, A fast All-sky Radiation Model for Solar applications with Narrowband Irradiances on Tilted surfaces (FARMS-NIT): part I. The clear-sky model, Sol. Energy 174 (2018) 691–702, https://doi.org/10.1016/j.solener.2018.09.056.

[9] C.A. Gueymard, REST2: High-performance solar radiation model for cloudless-sky irradiance, illuminance, and photosynthetically active radiation - validation with a benchmark dataset, Sol. Energy 82 (2008) 272–285, https://doi.org/10.1016/j.solener.2007.04.008.

[10] Y. Xie, M. Sengupta, C. Wang, A fast All-sky Radiation Model for Solar applications with Narrowband Irradiances on Tilted surfaces (FARMS-NIT): part II. The cloudy-sky model, Sol. Energy 188 (2019) 799–812, https://doi.org/10.1016/j.solener.2019.06.058.

[11] K. Papachristopoulou, I. Fountoulakis, A. Gkikas, P.G. Kosmopoulos, P.T. Nastos, M. Hatzaki, S. Kazadzis, 15-year analysis of direct effects of total and dust aerosols in solar radiation/energy over the Mediterranean Basin, Remote Sens. (Basel) 14 (2022) 1535, https://doi.org/10.3390/rs14071535.

[12] CAMS solar radiation time-series. https://doi.org/10.24381/5cab0912, 2020. (Accessed 8 September 2026).

[13] B. Gschwind, L. Wald, P. Blanc, M. Lefevre, M. Schroedter-Homscheidt, A. Arola, Improving the McClear model estimating the downwelling solar radiation at ground level in cloud-free conditions - McClear-v3, Meteorol.ogische Zeitschrift 28 (2019) 147–163, https://doi.org/10.1127/metz/2019/0946.

[14] C. Emde, R. Buras-Schnell, A. Kylling, B. Mayer, J. Gasteiger, U. Hamann, J. Kylling, B. Richter, C. Pause, T. Dowling, L. Bugliaro, The libRadtran software package for radiative transfer calculations (version 2.0.1), Geosci. Model Dev. 9 (2016) 1647–1672, https://doi.org/10.5194/gmd-9-1647-2016.

[15] B. Mayer, A. Kylling, Technical note: the libRadtran software package for radiative transfer calculations-description and examples of use, Atmos. Chem. Phys. 5 (2005) 1855–1877, https://doi.org/10.5194/acp-5-1855-2005.

[16] V. Salamalikis, P. Tzoumanikas, A.A. Argiriou, A. Kazantzidis, Site adaptation of global horizontal irradiance from the Copernicus Atmospheric Monitoring Service for radiation using supervised machine learning techniques, Renew. Energy 195 (2022) 92–106, https://doi.org/10.1016/j.renene.2022.06.043.

[17] F. Antonanzas-Torres, R. Urraca, J. Polo, O. Perpiñán-Lamigueiro, R. Escobar, Clear sky solar irradiance models: a review of seventy models, Renew. Sustain. Energy Rev. 107 (2019) 374–387, https://doi.org/10.1016/j.rser.2019.02.032.

[18] P. Ineichen, Validation of models that estimate the clear sky global and beam solar irradiance, Sol. Energy 132 (2016) 332–344, https://doi.org/10.1016/j.solener.2016.03.017.

[19] G. Xiu-Yan, L. Jie-Mei, Y. Yuan, T. He-Ping, Global horizontal irradiance prediction model considering the effect of aerosol optical depth based on the Informer model, Renew. Energy 220 (2024), https://doi.org/10.1016/j.renene.2023.119671.

[20] V. Salamalikis, I. Vamvakas, P. Blanc, A. Kazantzidis, Ground-based validation of aerosol optical depth from CAMS reanalysis project: an uncertainty input on direct normal irradiance under cloud-free conditions, Renew. Energy 170 (2021) 847–857, https://doi.org/10.1016/j.renene.2021.02.025.

[21] E.F.M. Abreu, C.A. Gueymard, P. Canhoto, M.J. Costa, Performance assessment of clear-sky solar irradiance predictions using state-of-the-art radiation models and input atmospheric data from reanalysis or ground measurements, Sol. Energy 252 (2023) 309–321, https://doi.org/10.1016/j.solener.2023.01.051.

[22] C.A. Gueymard, The SMARTS spectral irradiance model after 25 years: new developments and validation of reference spectra, Sol. Energy 187 (2019) 233–253, https://doi.org/10.1016/j.solener.2019.05.048.

[23] B. Reinhardt, R. Buras, L. Bugliaro, S. Wilbert, B. Mayer, Determination of circumsolar radiation from Meteosat Second Generation, Atmos. Meas. Tech. 7 (2014) 823–838, https://doi.org/10.5194/amt-7-823-2014.

[24] Y. Xie, J. Yang, M. Sengupta, Y. Liu, X. Zhou, Improving the prediction of DNI with physics-based representation of all-sky circumsolar radiation, Sol. Energy 231 (2022) 758–766, https://doi.org/10.1016/j.solener.2021.12.016.

[25] Y. Eissa, P. Blanc, H. Ghedira, A. Oumbe, L. Wald, A fast and simple model to estimate the contribution of the circumsolar irradiance to measured broadband beam irradiance under cloud-free conditions in desert environment, Sol. Energy 163 (2018) 497–509, https://doi.org/10.1016/j.solener.2018.02.015.

[26] T. Elias, N. Ferlay, G. Chesnoiu, I. Chiapello, M. Moulana, Regional validation of the solar irradiance tool SolaRes in clear-sky conditions, with a focus on the aerosol module, Atmos. Meas. Tech. 17 (2024) 4041–4063, https://doi.org/10.5194/amt-17-4041-2024.

[27] A. Driemel, J. Augustine, K. Behrens, S. Colle, C. Cox, E. Cuevas-Agulló, F.M. Denn, T. Duprat, M. Fukuda, H. Grobe, M. Haeffelin, G. Hodges, N. Hyett, O. Ijima, A. Kallis, W. Knap, V. Kustov, C.N. Long, D. Longenecker, A. Lupi, M. Maturilli, M. Mimouni, L. Ntsangwane, H. Ogihara, X. Olano, M. Olefs, M. Omori, L. Passamani, E. Bueno Pereira, H. Schmithüsen, S. Schumacher, R. Sieger, J. Tamlyn, R. Vogt, L. Vuilleumier, X. Xia, A. Ohmura, G. König-Langlo, Baseline Surface Radiation Network (BSRN): structure and data description (1992-2017), Earth Syst. Sci. Data 10 (2018) 1491–1501, https://doi.org/10.5194/essd-10-1491-2018.

[28] D.M. Giles, A. Sinyuk, M.G. Sorokin, J.S. Schafer, A. Smirnov, I. Slutsker, T.F. Eck, B.N. Holben, J.R. Lewis, J.R. Campbell, E.J. Welton, S.V. Korkin, A.I. Lyapustin, Advancements in the Aerosol Robotic Network (AERONET) version 3 database - automated near-real-time quality control algorithm with improved cloud screening for Sun photometer aerosol optical depth (AOD) measurements, Atmos. Meas. Tech. 12 (2019) 169–209, https://doi.org/10.5194/amt-12-169-2019.

[29] H.E. Beck, N.E. Zimmermann, T.R. McVicar, N. Vergopolan, A. Berg, E.F. Wood, Present and future Köppen-Geiger climate classification maps at 1-km resolution, Sci. Data 5 (2018) 180214, https://doi.org/10.1038/sdata.2018.214.

[30] I.F.S. Ecmwf, Documentation CY49R1 - Part VIII: atmospheric composition, in: IFS Documentation CY49R1, ECMWF, 2024, https://doi.org/10.21957/d13af18259.

[31] M.D. King, D.M. Byrne, A method for inferring total ozone content from the spectral variation of total optical depth obtained with a solar radiometer, J. Atmos. Sci. 33 (1976) 2242–2251, https://doi.org/10.1175/1520-0469(1976)033<2242:AMFITO>2.0.CO;2.

[32] T.F. Eck, B.N. Holben, J.S. Reid, O. Dubovik, A. Smirnov, N.T. O'Neill, I. Slutsker, S. Kinne, Wavelength dependence of the optical depth of biomass burning, urban, and desert dust aerosols, J. Geophys. Res. Atmos. 104 (1999) 31333–31349, https://doi.org/10.1029/1999JD900923.

[33] R. Perez, R. Seals, J. Michalsky, All-weather model for sky luminance distribution – preliminary configuration and validation, Sol. Energy 50 (1993) 235–245, https://doi.org/10.1016/0038-092X(93)90017-I.

[34] GUM, Evaluation of measurement data – guide to the expression of uncertainty in measurement. https://www.bipm.org/documents/20126/2071204/JCGM_100_2008_E.pdf, 2008. (Accessed 24 June 2025).

[35] M.D. Wilkinson, M. Dumontier, IjJ. Aalbersberg, G. Appleton, M. Axton, A. Baak, N. Blomberg, J.W. Boiten, L.B. da Silva Santos, P.E. Bourne, J. Bouwman, A. J. Brookes, T. Clark, M. Crosas, I. Dillo, O. Dumon, S. Edmunds, C.T. Evelo, R. Finkers, A. Gonzalez-Beltran, A.J.G. Gray, P. Groth, C. Goble, J.S. Grethe, J. Heringa, P.A.C. t Hoen, R. Hooft, T. Kuhn, R. Kok, J. Kok, S.J. Lusher, M. E. Martone, A. Mons, A.L. Packer, B. Persson, P. Rocca-Serra, M. Roos, R. van Schaik, S.A. Sansone, E. Schultes, T. Sengstag, T. Slater, G. Strawn, M.A. Swertz, M. Thompson, J. Van Der Lei, E. Van Mulligen, J. Velterop, A. Waagmeester, P. Wittenburg, K. Wolstencroft, J. Zhao, B. Mons, Comment: the FAIR Guiding Principles for scientific data management and stewardship, Sci. Data 3 (2016), https://doi.org/10.1038/sdata.2016.18.

[36] Y. Eissa, Y.-M. Saint-Drenan, G. Chesnoiu, P. Blanc, R. Jolivet, L. Ménard, ABC-Rad (AERONET-BSRN-CAMS-Radiation), mines Paris - PSL. https://doi.org/10.23646/384592a6-1d67-46f6-995d-8202bf51f190, 2025.

[37] X. Ceamanos, D. Carrer, J.L. Roujean, Improved retrieval of direct and diffuse downwelling surface shortwave flux in cloudless atmosphere using dynamic estimates of aerosol content and type: application to the LSA-SAF project, Atmos. Chem. Phys. 14 (2014) 8209–8232, https://doi.org/10.5194/acp-14-8209-2014.

[38] B. Mabasa, M.D. Lysko, H. Tazvinga, N. Zwane, S.J. Moloi, The performance assessment of six global horizontal irradiance clear sky models in six climatological regions in South Africa, Energies 14 (2021) 2583, https://doi.org/10.3390/en14092583.